Journal of Applied Nonlinear Dynamics 12(4) (2023) 723-738



Journal of Applied Nonlinear Dynamics

https://lhscientificpublishing.com/Journals/JAND-Default.aspx

Fractal Escape Basins for Magnetic Field Lines in Fusion Plasma Devices

Amanda C. Mathias[1], Leonardo C. de Souza[1], Adriane R. Schelin[2], Iberê L. Caldas[3], Ricardo L. Viana[1,3†]

[1] Departamento de Física, Universidade Federal do Paraná, 81531-990, Curitiba, Paraná, Brazil
[2] Departamento de Física, Universidade de Brasília, Brasília, DF, Brazil
[3] Instituto de Física, Universidade de São Paulo, 05508-090, São Paulo, São Paulo, Brazil

Submission Info

Communicated by Christos Volos
Received 14 March 2022
Accepted 8 August 2022
Available online 1 October 2023

Keywords

Escape basins
Magnetic field lines
Fractal structures
Tokamaks
Basin entropy

Abstract

Plasma confinement in fusion devices like Tokamaks depends on the existence of closed magnetic field lines with toroidal geometry. The magnetic field line structure in toroidal plasma devices is a Hamiltonian system, where the role of time is played by an ignorable coordinate. Nonsymmetrical perturbations lead to a nonintegrable hamiltonian system that can exhibit area-filling chaotic orbits. If exits are suitably positioned on a chaotic magnetic field line region, the Hamiltonian system becomes open and one is interested to know the corresponding escape basins, i.e., the sets of initial conditions for which the corresponding field lines escape through a given exit. From general mathematical arguments, it can be shown that these escape basins are fractal. In this paper, we investigate quantitatively fractal escape basins in the magnetic field line structure in Tokamaks described by an area-preserving map proposed by Balescu et al, using the uncertainty dimension to characterize the fractal structure of the magnetic field lines. We also use the concept of basin entropy in order to quantify the final state uncertainty, a relevant issue that arises when fractal basins are involved.

©2023 L&H Scientific Publishing, LLC. All rights reserved.

1 Introduction

The obtention of fusion plasma energy is a desideratum of a number of large undertakings throughout the world, the foremost example being the ITER (International Thermonuclear Experimental Reactor), currently being assembled in Southern France [1]. A long-term goal of ITER is to prove the feasibility of energy generation through thermonuclear fusion. ITER is designed to produce a deuterium-tritium plasma in which the fusion reactions are sustained through internal heating. It is expected that, from ~ 50 MW of input heating power, ITER will produce ~ 500 MW of fusion power: a ten-fold increase [2].

One of the major technical problems of generating a fusion plasma capable of delivering such power is the release of high-energy fusion products such as Helium atoms or impurity atoms created from

†Corresponding author.
Email address: viana@fisica.ufpr.br

ISSN 2164-6457, eISSN 2164-6473/$-see front materials © 2023 L&H Scientific Publishing, LLC. All rights reserved.
DOI:10.5890/JAND.2023.12.007

plasma-wall interactions [3]. The resulting heat and particle transport in ITER is expected to generate heat loads of $5-10\ MW/m^2$ that can damage the tokamak inner wall [4].

In order to mitigate this undesirable effect, the concept of divertor has been developed, which is a shaped metallic plate placed outside the plasma boundary to capture or divert particles escaping from the plasma [5]. Besides ITER, other currently operating tokamak devices like JET (Joint European Torus) and Alcator C-Mod also use divertors for this purpose [6, 7].

The basic idea underlying the operation of a divertor is that magnetic field lines can be arranged to deviate charged particles from the outer plasma region and direct them to a metallic plate. However, if the heat and particle loadings are not mitigated, the divertor plates could be damaged as well. In order to do so, it has been created a chaotic region of magnetic field lines in the outer plasma region. This helps to distribute such loadings over a larger area of the plates, creating the so-called magnetic footprints [8].

It was experimentally observed that magnetic footprints in divertor plates are not uniform and show a degree of self-similar behavior [9, 10]. In fact, the main point of the present paper is that magnetic footprints are a kind of fractal structure due to the nonintegrable nature of the magnetic field line structure [11]. Sanjuán and his collaborators have developed a useful tool to characterize fractal structures in dissipative and conservative dynamical systems, the so-called basin entropy [12, 13]. The latter is a measure of the final-state unpredictability of a dynamical system, given the fractal nature of the corresponding basins. If the system is dissipative, basins of attraction; if conservative, basins of escape [14]. Roughly speaking, the more complicated the basin structure, the higher the corresponding basin entropy will be. In the present work, we consider the characterization of fractal escape basins for magnetic field lines in a tokamak, using the basin entropy as the main tool and comparing our results with those obtained by the uncertainty fraction method [15, 16].

The numerical results we show in this paper are obtained by using as a magnetic field line model a two-dimensional area preserving map developed by Radu Balescu et al, the Tokamap [17]. The latter describes a Poincaré map for magnetic field lines in a Tokamak, using few parameters, which has been often used as a simple model for the study of chaotic trajectories related to nonsymmetric perturbations in Tokamaks. Previously we have made a similar analysis in a field line map restricted to a particular example, namely of a Tokamak with magnetic limiter [18]. In the present paper we consider the Tokamap, which describes a more general situation, since it represents a paradigm of nonsymmetric perturbations in Tokamaks. In this sense, the Tokamap is for plasma physics what the standard map represents for Hamiltonian dynamics.

This paper is organized as follows: in Section II we outline the basics of the magnetic field line structure in a tokamak, emphasizing the Hamiltonian nature of the equations. Section III presents the area-preserving two-dimensional map proposed to investigate the magnetic field line structure. In Section IV we present some numerical examples of escape basins for field lines exiting the plasma through small rectangular openings, and compute the corresponding connection lengths, directly related to the escape times. Section V reviews the method of computing the dimension of the escape basin boundary using the uncertainty fraction method. Section VI is devoted to the same characterization but now using basin and basin boundary entropies. Finally, in the last Section we report our Conclusions.

2 Magnetic field structure in a Tokamak

The Tokamak is a toroidal device for the magnetic confinement of a high-temperature plasma using two main magnetic fields: the toroidal field $\mathbf{B}_T$ created by external coils and the poloidal field $\mathbf{B}_P$, generated by the plasma itself. The equilibrium field $\mathbf{B} = \mathbf{B}_T + \mathbf{B}_P$ has helical magnetic lines of force. These field lines lie on toroidal surfaces called magnetic surfaces. The magnetic surface with zero volume is called magnetic axis. A surface quantity ψ is defined so as to take on a constant value on a magnetic surface,

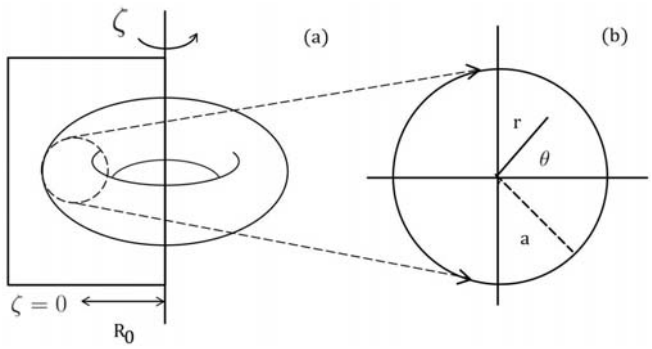


Fig. 1 (a) Schematic figure showing the basic geometrical features of a Tokamak. (b) Coordinates in a surface of section.

such that [19]

$$\mathbf{B} \cdot \nabla \psi = 0. \tag{1}$$

Fig.1(a) depicts the basic tokamak geometry which we will use in this paper. We denote by R_0 the distance between the magnetic axis and the symmetry (vertical) axis, and by ζ the toroidal angle, which is measured along the long way around the torus. If the toroidal vessel has circular cross section, a field line point on the corresponding plane (constant ζ) can be described by polar coordinates (r, θ) with center on the magnetic axis position [Fig.1(b)], where θ is called the poloidal angle. Without loss of generality, we assume that θ is normalized such that $0 \leq \theta < 1$. Moreover, we can choose $\psi = (r/a)^2$, where a is the plasma minor radius, and use (ψ, θ, ζ) as a convenient coordinate system for magnetic field lines [20]. The magnetic axis and the plasma edge are located at $\psi = 0$ and $\psi = 1$, respectively.

In this system, the magnetic field line equations can be expressed in a canonical form

$$\frac{d\psi}{d\zeta} = -\frac{\partial H}{\partial \theta}, \tag{2}$$

$$\frac{d\theta}{d\zeta} = \frac{\partial H}{\partial \psi}, \tag{3}$$

where (ψ, θ) are the canonically conjugated variables, the toroidal angle ζ plays the role of time and H is the corresponding field line Hamiltonian. This fact enables us to investigate magnetic field lines structure in toroidal plasma devices using the powerful tools of Hamiltonian dynamics, like perturbation theory, KAM theorem, and so on.

In the equilibrium (unperturbed) situation, H does not depend on the "time" ζ, and thus the one-degree-of-freedom Hamiltonian system is integrable. It is often the case that H is a function of ψ only, such that the canonical Eqs. (2)-(3) read

$$\frac{d\psi}{d\zeta} = 0, \tag{4}$$

$$\frac{d\theta}{d\zeta} = \frac{\partial H}{\partial \psi} = \frac{1}{q(\psi)}, \tag{5}$$

where $q(\psi)$ is called the safety factor. In this situation, (ψ, θ) are actually action-angle variables, and the magnetic surfaces $\psi = \text{const.}$ coincide with the invariant tori of the integrable Hamiltonian system.

We adopt the standard Tokamak equilibrium magnetic field model [21]

$$\mathbf{B} = \mathbf{B}_P + \mathbf{B}_T = \frac{B_0 r}{q(r) R_0} \hat{\mathbf{e}}_r + \frac{B_0}{1 + (r/R_0)\cos\theta} \hat{\mathbf{e}}_\zeta, \tag{6}$$

where $\mathbf{B}_0$ is the toroidal field at magnetic axis. The unit vectors $\hat{\mathbf{e}}_r$ and $\hat{\mathbf{e}}_\zeta$ refer to the radial and toroidal directions in Fig.1(a), respectively. Moreover, a and R_0 denote the minor and major plasma radii, and the Tokamak aspect ratio, $A = R_0/a$, is assumed to be large enough that the safety factor depends only on the radial distance:

$$q(r) = \frac{d\zeta}{d\theta} = \frac{rB_0}{R_0 B_\theta(r)}, \tag{7}$$

where we used the magnetic field line equations in this local coordinate system.

Typical parameter values for the tokamak TCABR, operating at the Institute of Physics, University of São Paulo, Brazil, are [22] $R_0 = 0.61\ m$, $a = 0.18\ m$, and $B_0 = 1.1\ T$. The safety factor radial profile $q(r)$ can be tailored to fit density and temperature measurements. We consider the following expression for the safety factor, expressed in terms of $\psi = (r/a)^2$ as [21]

$$q(\psi) = \frac{4q_0}{(2-\psi)(2-2\psi+\psi^2)}, \tag{8}$$

where q_0 is the safety factor at magnetic axis. In order to avoid dangerous plasma instabilities it is convenient to assume $q_0 = 1$. Hence the safety factor at plasma edge is $q(\psi = 1) = 4$, which is consistent with measurements of the plasma current, electron density and temperature. For the TCABR Tokamak typical values of these parameters are respectively [23] $I_p = 100\ kA$, $n_e = (1.0-4.0)\times 10^{19}\ m^{-3}$, $T_e = (0.2-1.5)\ eV$.

Many physical reasons, like error fields, external magnetic fields or instabilities, cause "time"-dependent perturbations that turn the magnetic field line into a non-integrable system. The Hamiltonian reads now $H = H(\psi,\theta,\zeta)$. If the perturbation is weak enough, the Hamiltonian can be cast into the form of a quasi-integrable system

$$H(\psi,\theta,\zeta) = \int_0^\psi \frac{d\psi'}{q(\psi')} + \varepsilon H_1(\psi,\theta,\zeta), \tag{9}$$

where $\varepsilon \ll 1$ represents the perturbation strength.

3 Magnetic field line map

In plasma physics applications, after deriving the perturbing Hamiltonian from some physical model of non-integrable perturbation, the magnetic field line behavior is obtained from numerically integrating Hamilton Eqs. (2)-(3). This is a time-consuming task specially if long-time integrations are needed, so a considerable simplification emerges from using a magnetic field line map [24].

The coordinates of the nth intersection of a given magnetic field line with the surface of section at $\zeta = 0$ are denoted by (ψ_n, θ_n). A Poincaré map relates the coordinates of two consecutive intersections of a field line with this plane, namely

$$\psi_{n+1} = f(\psi_n, \theta_n), \tag{10}$$

$$\theta_{n+1} = g(\psi_n, \theta_n), \tag{11}$$

where the functions (f, g) are related to the field line Hamiltonian (9) and must fulfill some conditions of physical consistency.

The condition $\nabla\cdot\mathbf{B} = 0$ implies the conservation of the magnetic flux. An important consequence is that the Poincaré map (10)-(11) is area-preserving in the surface of section, that is,

$$\begin{vmatrix} \partial f/\partial\psi & \partial f/\partial\theta \\ \partial g/\partial\psi & \partial g/\partial\theta \end{vmatrix} = 1. \tag{12}$$

Moreover, from the definition $\psi = r^2/a^2$, there follows that $\psi_n \geq 0$ for any value of the discrete time n (measured in number of toroidal field line turns). In particular, this must hold for $n = 0$ as well.

Balescu and coworkers have proposed a Poincaré map satisfying these conditions, called tokamap, which reads [17]

$$\psi_{n+1} = \frac{1}{2}\{P(\psi_n, \theta_n) + \sqrt{P(\psi_n, \theta_n)^2 + 4\psi_n}\} \tag{13}$$

$$P(\psi_n, \theta_n) = \psi_n - 1 - \frac{k}{2\pi}\sin(2\pi\theta_n), \tag{14}$$

$$\theta_{n+1} = \theta_n + \frac{1}{q(\psi_n)} - \frac{k}{4\pi^2}\frac{1}{(1+\psi_{n+1})^2}\cos(2\pi\theta_n), \qquad (\mathrm{mod}1), \tag{15}$$

$$q(\psi) = \frac{4}{(2-\psi)(2-2\psi+\psi^2)}. \tag{16}$$

The perturbation strength k is the only tunable parameter in the tokamap (13)-(16). In a physical setting, where the non-symmetrical perturbation is produced by a vacuum magnetic field created by helical windings, k can be regarded as proportional to the current flowing through the winding, for example [20]. This kind of perturbations is also related to plasma instabilities [25]. Field line maps where the non-integrable perturbation term comes from a physical model have been extensively studied [26, 27]. The tokamap has the special feature of being consistent with physical requirements, whereas the perturbation is kept simple by choosing a sinusoidal term. More general perturbations can be regarded, in this sense, as expansions in trigonometric functions, in such a way that the tokamap is a simple model, but representative of more complicated situations occurring in physical applications. We have recently used this model to investigate the dissipative effect of collision in the magnetic field line structure [28].

In the limit of vanishing perturbation ($k = 0$) we have $P(\psi_n) = \psi_n - 1$ and the tokamap reduces to a simple twist map,

$$\psi_{n+1} = \psi_n \tag{17}$$

$$\theta_{n+1} = \theta_n + \frac{1}{q(\psi_n)}, \qquad (\mathrm{mod}1), \tag{18}$$

which is known to describe an integrable system. This map satisfies the twist condition, provided the safety factor is monotonic, i.e., does not present extrema. This is the case, for example, of the safety factor given by (8). Non-monotonic safety factor profiles have also been considered by Balescu, who proposed the so-called revtokamap as a non-twist version of the map (13)-(15) [29].

In the following, we will work in regimes where $k > 0$, representing non-integrable perturbations on magnetic field line structure. Figs.2(a)-(d) exhibit phase portraits of the tokamap for increasing values of the parameter k. Physically this could be realized, e.g. by increasing the current flowing through external wires wound around the Tokamak vessel or enhancing a given error field caused by some misalignment of external currents [30]. It is well-known that these effects are potentially generators of complex field line structures. Although the canonical variables ψ and θ are actually a kind of polar coordinates, the visualization of phase portraits improves by using a rectangular projection, in which $0 \leq \theta < 1$ is the poloidal angle and $0 \leq \psi \leq 1$ is a radial-like coordinate. The lines $\psi = 0$ and $\psi = 1$ represent the magnetic axis and tokamak boundary, respectively.

For small k, we have invariant curves with some degree of distortion and also some periodic island chains [Fig.2(a)]. According to KAM theory, the distorted invariant curves correspond to irrational tori of the unperturbed system, whereas the island chains appear due to the destruction of rational tori, in accordance with Poincaré-Birkhoff theorem [31]. The observed distortion of both invariant tori

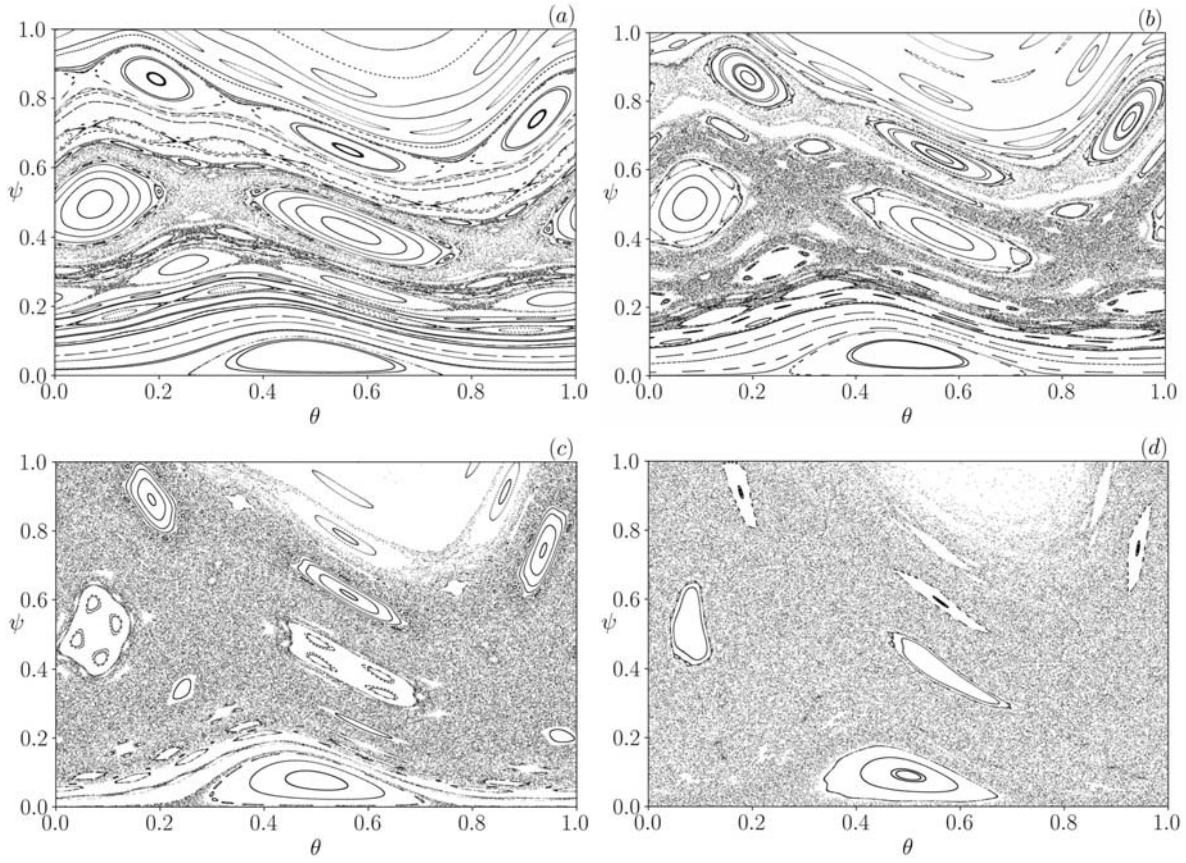


Fig. 2 Phase portraits of the Tokamap for (a) $k = 3.5$, (b) $k = 4.0$, (c) $k = 5.0$. (d) $k = 6.0$.

and island chains increases with k [Fig.2(b)]. Moreover, the width of the island chains also increases with this parameter, allowing the visualization of even more periodic islands.

Physically the invariant tori represent dikes preventing field line diffusion, and the magnetic islands also limit radial excursions. The homoclinic intersections in the vicinity of the islands separatrices are responsible for the creation of a chaotic layer therein. However, even in this case, the field line excursions are limited by the bounding invariant curves above or below. It is important, however, to emphasize that the word chaos applies to the magnetic field line structure in a peculiar way: since the magnetic fields are strictly static in time, one considers the field line dynamics in a Lagrangian sense as being parameterized by the toroidal coordinate, which plays the role of time. Accordingly, field line chaos means that two initial conditions chosen in an area-filling region, generate field lines that separate at an exponential rate, which we can interpret as the maximal Lyapunov exponent [32].

As the value of k increases, the chaotic layers belonging to neighbor island chains overlap and give rise to wider chaotic layers [Fig.2(c)] which can increase so as to occupy practically all the available phase portrait, except for the vicinity of the magnetic axis. If k further increases, even the latter region is filled with chaotic orbits [Fig.2(d)], and there are remnants of periodic islands embedded in the large chaotic sea.

The chaotic saddle is a non-attracting invariant chaotic set which is the key structure underlying the chaotic dynamics displayed by the Tokamap, hereafter denoted simply by $\mathbf{F}$. The stable manifold of a point P in this invariant chaotic set is the set of points Q whose forward iterates asymptotically approach each other, i.e. $|\mathbf{F}^n(P) - \mathbf{F}^n(Q)| \to 0$ as $n \to \infty$. Analogously, the unstable manifold of a point P is the set of points Q whose backward iterations asymptotically approach each other: $|\mathbf{F}^{-n}(P) - \mathbf{F}^{-n}(Q)| \to 0$ as $n \to \infty$. We obtained numerical approximations of both manifolds by using the sprinkler method [33]: a

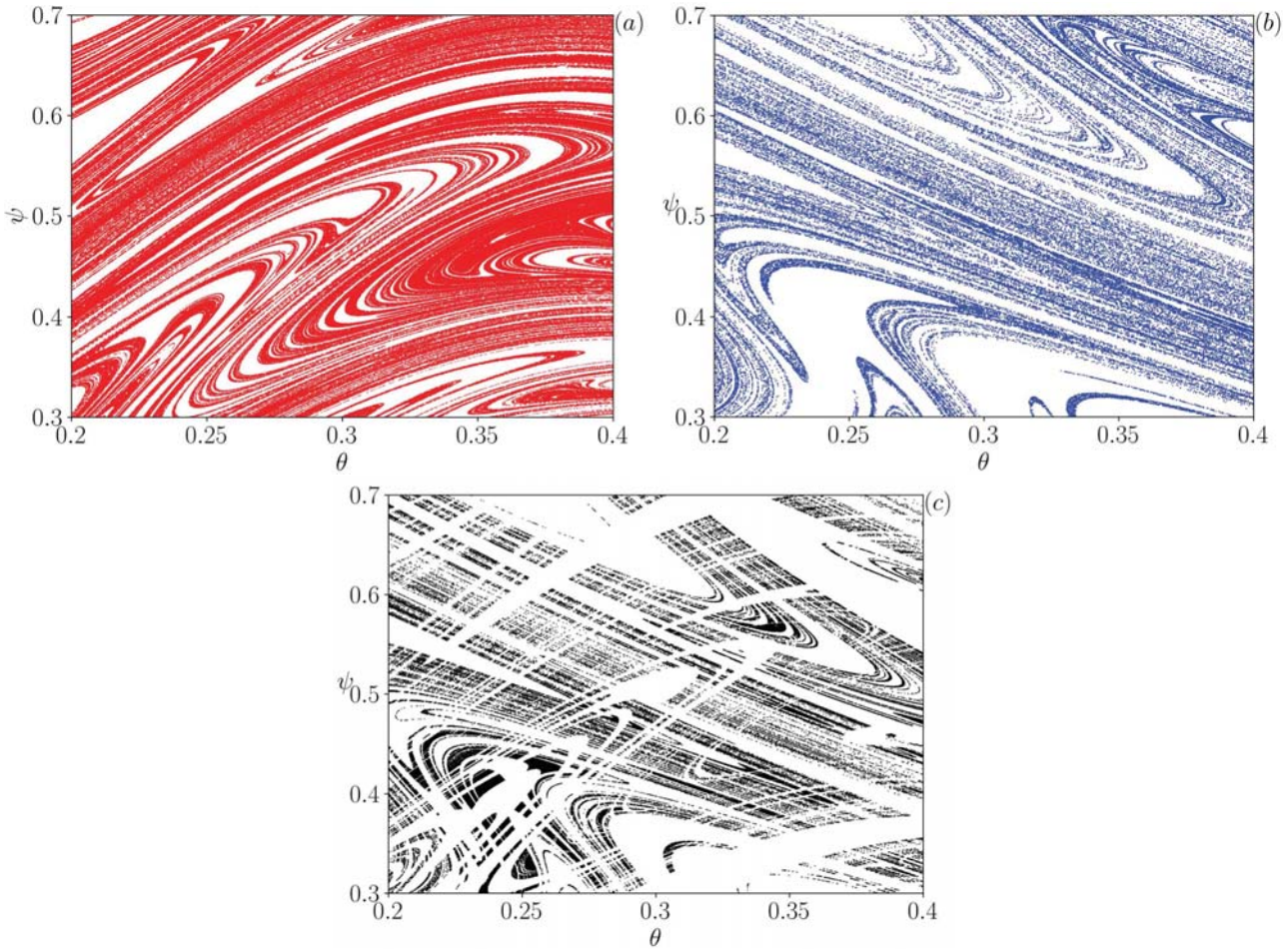


Fig. 3 (a) Stable manifold, (b) Unstable manifold, (c) Chaotic saddle of a region in the midst of the chaotic region for the Tokamap with $k = 2\pi$.

given phase plane region $\mathscr{R}$ is partitioned into a fine grid of points, and each point is iterated m times. If m is large enough, trajectories (field lines) that remain in the region $\mathscr{R}$ after m iterates are numerical approximations of the stable manifold of the invariant set. Moreover, the m-th iterates of the initial conditions are approximations of the unstable manifold. An intermediate number of iterates (like $m/2$) is an approximation of the chaotic saddle itself.

Our results for the Tokamap at $k = 2\pi$ are shown in Fig.3: a fine mesh of 1000×1000 has been used in a region contained in the chaotic region. Each mesh point was iterated $m = 30$ times, and the numerical approximations of the stable and unstable manifolds are depicted in Figs.3(a) and (b), respectively. The chaotic saddle is shown in Fig.3(c).

4 Escape basins and connection lengths

In its original form, Eqs. (13)-(15), the Tokamap represents a closed Hamiltonian system. The restriction $\psi_n \leq 1$ for the orbits generated by the Tokamap is physical rather than a mathematical one, such that one could consider orbits with $\psi_n > 1$ as well. This dynamical system can be opened by considering the possibility of field line escape through one or more exits [34]. Once a given map orbit hits one of these exits, it is assumed lost forever and we stop iterating the map.

These exits can be, for example, divertor plates used to mitigate plasma-wall interactions due to

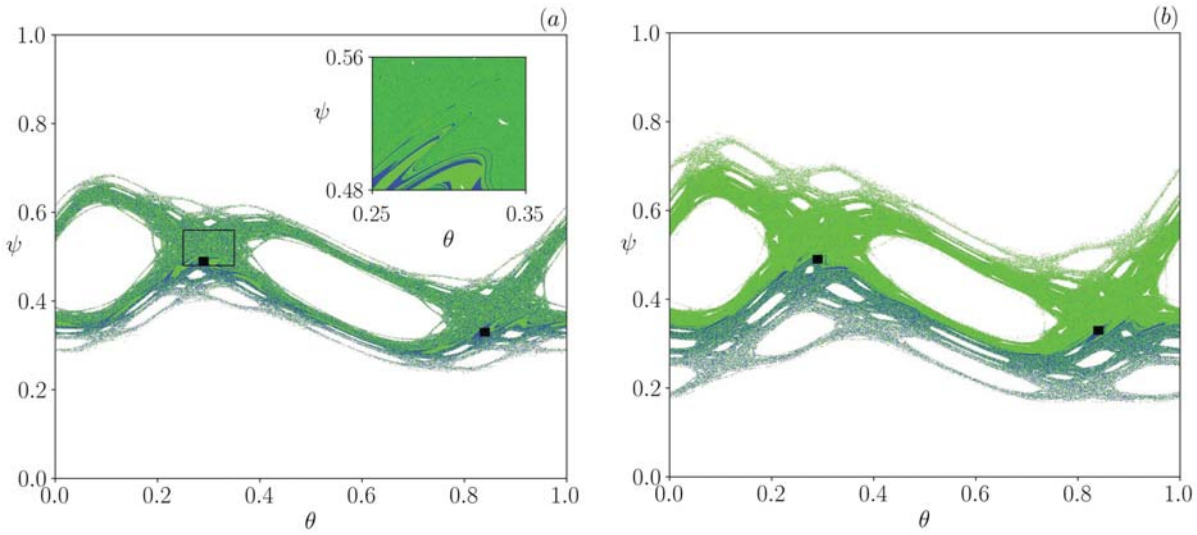


Fig. 4 Escape basins of the exits L and R, for (a) $k = 3.50$ and (b) $k = 3.75$. The inset in (a) is a magnification of a box surrounding L.

energetic particles, as discussed in the Introduction. However, the precise locations of these divertor plates depend chiefly on the Tokamak design, and it is a difficult technological problem that has to be tackled case-by-case [35]. In the present work, however, we are more concerned with the dynamical aspects of the problem, since we are interested in investigating the fractal structures that appear due to the chaotic nature of some orbits. Hence we will choose exits in a convenient way from the point of view of a better visualization of the fractal structures sought after. Once we identify these structures therein, it is rather simple to extend this discussion to exits in actual divertor plates located outside the plasma, between its boundary and the tokamak vessel wall.

In this section, we will consider two of such exits placed in the plasma core, represented by two small rectangles in Figs.4(a) and (b): let us call these exits L and R, since they are located at the left and right of the line $\theta = 0.5$, respectively. The corresponding escape basins, denoted by $\mathsf{B}(\mathsf{L})$ and $\mathsf{B}(\mathsf{R})$, are the sets of initial conditions that generate orbits escaping through L and R, respectively. If these exits are located at uninteresting positions, like within a periodic island, it is unlikely that there will be points belonging to either L or R. We thus choose the exits within an area-filling chaotic orbit.

This is the case of Fig.4(a), for $k = 3.50$, where the exits are placed in the core of a chaotic orbit [see Fig.2(d)], and where basins of L and R are those regions painted in green and blue, respectively. The mixing of the escape basins $\mathsf{B}(\mathsf{L})$ and $\mathsf{B}(\mathsf{R})$ is clearly seen, especially in the vicinity of the exits themselves. A magnification of a box in this vicinity shows a finger-like structure of blue basin filaments embedded in the green basin. A similar structure appears for $k = 3.75$ [Fig.4(b)].

This finger-like structure shows up due to the dynamical behavior of the map iterates in a chaotic orbit. More specifically, we concentrate on the boundary S between the escape basins $\mathsf{B}(\mathsf{L})$ and $\mathsf{B}(\mathsf{R})$. Similar to that occurring for basins of attraction, the escape basin boundary is the closure of the stable manifold of an unstable periodic orbit embedded in an area-filling chaotic orbit. We represent schematically this situation in Fig.5: let P be an unstable periodic orbit (a saddle point) embedded in a chaotic orbit of the map $\mathbf{F}$, and we denote by $W^s(P)$ and $W^u(P)$, respectively, the stable and unstable manifolds emanating from P . The extremely complicated set of interactions between these manifolds constitutes the so-called homoclinic tangle.

Let S be a segment of the escape basin boundary intercepting the unstable manifold $W^u(P)$. The backward images of this segment, as $\mathbf{F}^{-1}(S)$ and $\mathbf{F}^{-2}(S)$, become increasingly thin and elongated spaghetti-like fingers accumulating at the stable manifold $W^s(P)$. This occurs because the intersec-

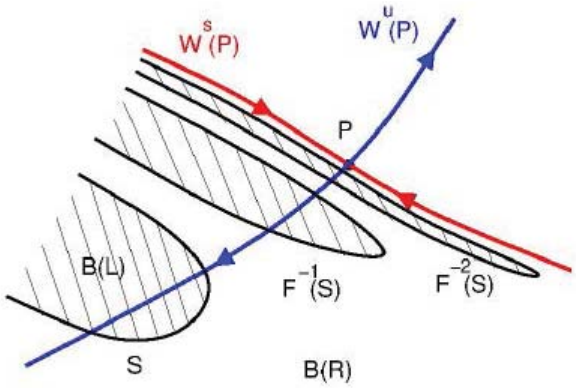


Fig. 5 Schematic figure showing the accumulation of escape basin filaments at the stable manifold of an unstable periodic orbit embedded in a chaotic orbit of the map.

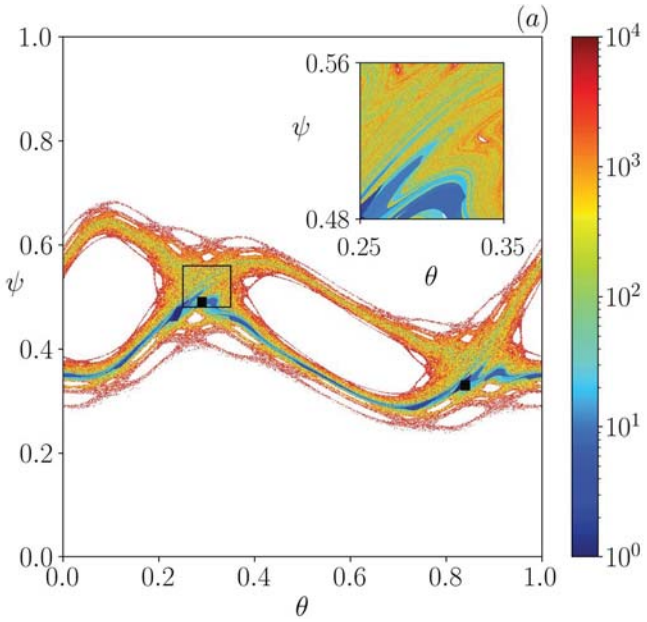


Fig. 6 Connection length (in colorscale) for the Tokamap with $k = 3.5$. The inset is a magnification of a box surrounding L.

tions between S and $W^u(P)$ converge to the unstable orbit P at a rate given, in its neighborhood, by the corresponding eigenvalue of the tangent map $\mathbf{DF}(P)$ [36]. The fingers become elongated due to the area conservation requirement of the Tokamap $\mathbf{F}$. The numerical approximations of the invariant manifolds shown in Fig.3 explain the complicated structure of the escape basin boundaries.

The mixing of the escape basins has observable consequences in terms of plasma physics applications. In Fig.6 we plot (in a color scale) the escape "time" of orbits with initial conditions picked up from the chaotic region, which is the number of map iterations it takes for a given orbit to escape through either one of the exits. In the plasma physics literature it is also named connection length since we are actually measuring the length of a magnetic field line from its initial condition to the point it exits from the Tokamak [37].

The initial conditions with higher escape times (more than 10^3 iterations) are located near the island boundaries, which is a consequence of the stickiness behavior characteristic of these regions. Such orbits correspond to magnetic field lines with large connection lengths (remember that each map iteration represents a complete particle turn around the Tokamak). Considering that, in a first approximation,

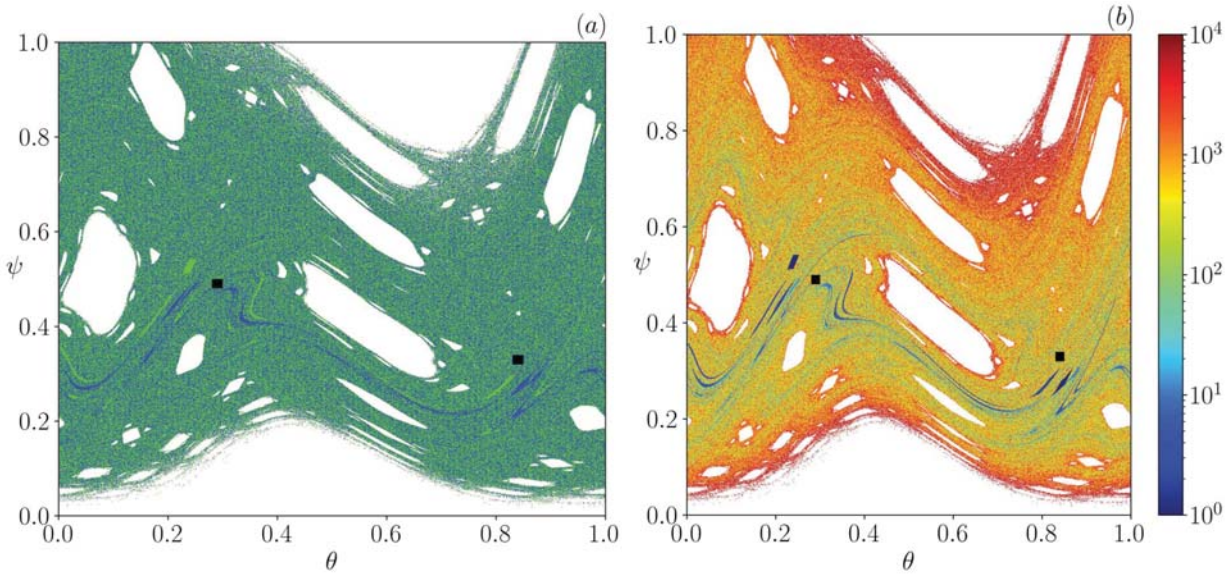


Fig. 7 (a) Escape basins of the exits L and R, for $k = 5.0$. (b) Connection length (in colorscale) for the same situation.

plasma particles (electrons and positive ions) gyrate along the magnetic field lines, large connection lengths are related to particles which make a large number of turns along the Tokamak before exiting. Since these particles collide with other plasma particles, we expect highly energetic particles from field lines with large escape times. Such high-energy particles are thus responsible for substantial heat loading on the divertor plates positioned at the chosen exits [38].

We expect that the finger-like structure of the escape times exhibited by Fig.6 brings about a similarly complicated structure of the heat patterns measured in divertor plates. This fact has been actually observed in a variety of Tokamak experiments. Jakubowski et al has measured the power deposition on divertor plates at the DIII-D Tokamak with resonant magnetic perturbations used to suppress the so-called edge localized modes in plasmas subjected to high-confinement mode (H-mode) [9]. Similar investigations have been made for magnetic perturbations due to a dynamic ergodic divertor [10]. The complex structure of heat patterns has been assigned to the situation depicted in Fig.5 [39]. The mixture of long and short connection length field lines is responsible for the fingerlike structures observed in the deposition patterns [40, 41].

5 Uncertainty dimension

The chaotic region widens considerably by increasing the value of k. In Fig.7(a) and (b), we depict the escape basins and the escape time, respectively, for $k = 5.0$. The chaotic region has increased its size by engulfing periodic islands in both sides, such that it intercepts the plasma boundary. A further increase of k turns the chaotic region even larger, and the corresponding escape basins are likewise distributed over it.

A close inspection of Fig.7(a) shows that the escape basins are mixed throughout the chaotic region. However, the basins are not disconnected as it might seem. In fact, the escape basins are intertwined in arbitrarily fine scales, what is only possible if the basins themselves and their common boundary are fractals. The existence of fractal basin boundaries has been long-known to be connected with basins of attraction, and its fractal nature comes from a mechanism similar to that described here.

A quite direct way to characterize the fractality of the escape basin boundaries is to compute their

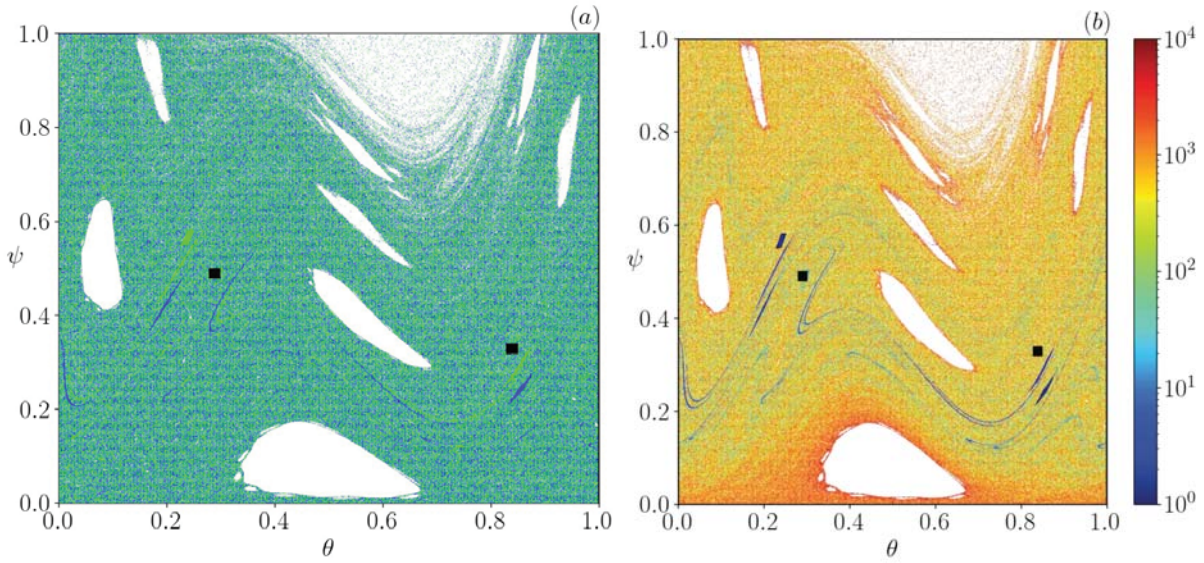


Fig. 8 (a) Escape basins of the exits L and R, for $k = 6.0$. (b) Connection length (in colorscale) for the same situation.

uncertainty dimension. Since any initial condition in the phase space (in the present case, the Poincaré surface of section) is known up to a given uncertainty ε, we can think of it are being represented by a disk of radius ε centered at the point (ψ_0, θ_0). If this ε-disk intercepts the escape basin boundary, one cannot say a priori to which exit will escape the orbit generated by that initial condition. We call this final-state uncertainty [15, 16].

We consider a number of randomly chosen initial conditions in a given phase plane region containing a significant piece of the escape basin boundary. The initial condition at the center of each ε-ball is iterated until it escapes through L or R exits. A second initial condition is randomly chosen inside this ε-ball, and it is again iterated until it escapes. If this second initial condition leaves through a different exit, it will be called ε-uncertain. Notice that, for each escaping initial condition, we consider two other initial conditions inside the ε-ball. Accordingly, choosing more initial conditions reduces the probability of getting false-negatives.

The uncertain fraction $f(\varepsilon)$ is the number of ε-uncertain conditions divided by their total number. It is expected to scale with ε as $f(\varepsilon) \sim \varepsilon^{\alpha}$, where α is the uncertainty exponent. The latter is given by $\alpha = D - d$, where $D = 2$ is the phase plane dimension and d is the box-counting dimension of the escape basin boundary. If the escape basin boundary is a smooth curve ($d = 1$), then $\alpha = 1$ and the uncertain fraction is simply proportional to ε, as it should be (ε-disks close to the basin boundary are more likely to intercept the boundary). However, it the basin boundary is fractal, then $0 < \alpha < 1$, such that its dimension is $1 < d < 2$.

A fractal escape basin boundary turns out to be a strong limitation to the capability of determining the final state of the map orbit. Let us suppose, for example, that $\alpha = 0.01$, implying a basin boundary with dimension $d = 1.99$, i.e., almost an area-filling curve (akin to the Hilbert or Peano curves, for instance). Let us imagine that a great deal of effort is spent in diminishing the uncertainty by half. In this case, the uncertain fraction becomes

$$f(\varepsilon') \sim \left(\frac{1}{2}\right)^{\alpha} f(\varepsilon) \approx 0.9931 f(\varepsilon),$$

which represents a decrease of less than 1% in the final-state uncertainty! We see that such an enormous effort to decrease the initial condition uncertainty would have a small effect on the final-state uncertainty.

Table 1 Uncertainty exponents and dimensions for the escape basin boundaries of the Tokamap.

k	α	d	global error
3.5	0.00037	1.9996	0.0006
4.0	0.00015	1.9998	0.0002
4.5	0.00031	1.9997	0.0007
5.0	0.00034	1.9997	0.0007
5.5	0.00045	1.9995	0.0009
2π	0.00078	1.9992	0.0010

The numerical results were obtained for a grid of 5000×5000 initial conditions placed in the midst of the chaotic region displayed in the phase portrait of the Tokamap for a given value of the non-integrability parameter k. We iterated each initial condition 10^4 times according to the algorithm described above. If the initial condition does not escape at this time it is removed from the computation, since the initial condition may be within a periodic island. Some numerical error is expected, though, because there are orbits with escape times larger than 10^4. We assume that these orbits are relatively too few to influence the final results.

For each value of ε, we repeat ten times the computation of the uncertainty fraction, the local error being the standard deviation of the results. Ten values of ε are used to make a diagram of $\log f(\varepsilon)$ versus ε, and the uncertainty dimension was determined by a least- squares fit. The global error is the average local error for each ε. Our results, for different values of k, are in Table 1. The uncertainty dimension varies very little with k and is very close to 2.0. In all those cases, the basin boundary is extremely involved and approaches an area-filling curve as k increases to 2π. These results point to an extreme fractal escape basin structure, but the information provided by the uncertainty dimension is insufficient to characterize the role of the parameter k. This is an example of a situation in which the traditional approaches are not very illuminating, and new concepts are necessary, like the basin and basin boundary entropies.

6 Basin entropy

The fractal nature of the escape basins and their boundaries, suggested by the explicit computation of their uncertainty dimensions, can also be investigated using the concept of basin entropy, introduced by Daza et al [12,13]. Basin entropy, when applied to escape basins, measures the degree of final-state uncertainty produced by the fractality of the escape basin boundary, using basic ideas from information theory.

Let us consider a bounded region $\mathscr{R}$ of the phase plane in which an area-filling chaotic orbit exists, perhaps with periodic islands embedded. We cover $\mathscr{R}$ with a fine mesh, such that each grid point is assigned to a random variable with the different exits as the possible results. The corresponding basin entropy is obtained from computing information entropy for this set. In the case of an arbitrary number N_A of exits, we consider that the fine mesh of N^2 grid cells covering $\mathscr{R}$ has grid size, with initial conditions (ψ_0, θ_0) chosen at each grid cell. To each initial condition, we assign a color labeled from 1 to N_A, and the colors within the grid cell are randomly distributed according to a probability p_{ij} for the jth color assigned to the ith grid cell. If the chaotic orbits of the magnetic field line map are statistically independent, the basin entropy of the ith grid cell is defined as

$$S_i = -\sum_{j=1}^{m_j} p_{ij} \log p_{ij}, \tag{19}$$

where $1 \leq m_i \leq N_A$ is the number of colors inside the ith grid cell.

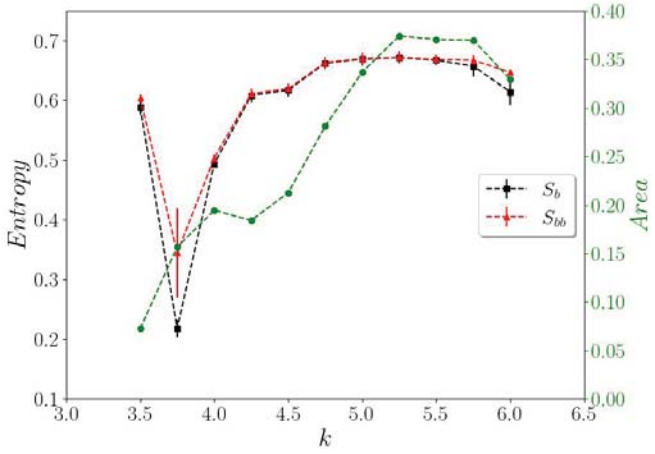


Fig. 9 Entropy of the escape basin (black squares) and the escape basin boundary (red triangles) as a function of the parameter k for the Tokamap. The relative area of the green basin is represented by green circles.

Since this quantity is extensive, the total grid entropy is the sum of (19) for all grid cells. Finally the basin entropy results from dividing by the number of grid cells:

$$S_b = \frac{1}{N}\sum_{i=1}^{N} S_i. \tag{20}$$

If we have a single exit ($N_A = 1$) the basin entropy turns zero, which means no uncertainty with respect to the final state, since there is a unique escape basin. On the other extreme, let us consider N_A equiprobable exits: the probability is the same for each grid cell. In this case the corresponding basins are densely mixed and have entropy $S_b = \log N_A$. Another quantity of interest is the basin boundary entropy, which quantifies the final-state uncertainty restricted to the escape basin boundary. In this case, we apply (20) by replacing the total number of grid cells N by the number of grid cells N_b containing more than one color: $S_{bb} = S/N_b$.

The fractal structures described so far refer to $N_A = 2$ exits, for which the corresponding escape basins have been painted green and blue, respectively. The bounded region in the phase plane used to compute the basin entropy is the rectangle $0 \le \psi \le 1$, $0 \le \theta < 1$ covered with a grid of 1000×1000 points. Those grid cells containing pieces of the periodic islands are discarded from the computation, since the initial conditions therein are not likely to escape. For those initial conditions centered at each box we iterate the Tokamak 10^4 times until they escape through exits L or R. If the orbit does not leave after this maximum time, the corresponding initial condition is also discarded.

For each grid cell, we compute the number n_1 (resp. n_2) of points that escape through exit L (resp. R), such that the probabilities for the ith box are

$$p_{i1} = \frac{n_1}{n_1 + n_2}, \qquad p_{i2} = \frac{n_2}{n_1 + n_2}, \tag{21}$$

and the entropy of that grid cell is $S_i = -p_1 \log p_1 - p_2 \log p_2$. The basin entropy S_b results from summing S_i over all boxes for which all initial conditions escape and dividing by their number. The computation of the basin boundary entropy S_{bb} discards those boxes for which either $p_1 = 0$ or $p_2 = 0$. In other words, for computing S_{bb} we consider only those grid cells which intercept the escape basin boundary.

Our results are summarized in Fig.9, where we plot the entropy of the exit L (green) basin for different values of the parameter k of the Tokamap, as well as the corresponding basin boundary entropy. The results for the exit L (blue) basin are practically the same as those of the R basin. We also indicate in Fig.9 the relative area of the L (green) basin, defined as the number of grid points

belonging to that basin divided by the total number of boxes in the grid. A similar computation can be done as well for the blue basin, but the sum of the corresponding relative areas is not equal to the unity, since a part of the region is occupied by points that do not escape (for example, inside periodic islands).

For $k = 3.50$ both the basin and basin boundary entropies take on similar values about 0.6, which already indicates a considerable degree of mixing between the escape basins, followed by a dip to smaller entropies when $k = 3.75$. The relative area of the green basin has increased from 0.22 to 0.35. In Figs.4(a) and (b) we compare both escape basins for these two values of k. The increase in the green area (as well as the blue area) results from the destruction of KAM tori and the consequent enlargement of the chaotic region. However, due to the placement of the two exits (indicated by the squares) there is a preference for exiting through the R basin, thus decreasing the complexity of the green basin.

However, for higher values of k, the basin and basin boundary entropies increase with k, indicating a trend for increasing complexity. This trend is not clearly shown by the uncertainty dimension, however (see Table 1), since the values are too close to each other within the global error. For $k > 4.75$, the entropies reach a saturation as well, with values close to the predicted maximum $S = \log 2$, which would represent a completely mixed basin structure. Notice also that the basin boundary entropy S_{bb} is always slightly larger than S_b , which is expected since the number of grid cells containing the boundary is smaller than the total number of grid cells considered for basin entropy. It is also noteworthy that the area of the green basin increases with k, achieving a maximum of about 0.37.

Although this would suggest some correlation between the entropies and the relative size of the basins, we observe that for $k = 3.75$ the entropy has actually decreased, even though the relative area continues to grow. As a matter of fact, the fractality of the escape basin is related to the invariant manifold, rather than to the sheer size of the basins themselves.

7 Conclusions

The emergence of chaotic behavior in plasma physics problems is a natural consequence of their intrinsic nonlinear character. Only recently has this chaoticity been recognized as a major problem in the research towards controlled nuclear fusion using magnetic confinement, chiefly through Tokamaks. In particular, the existence of chaotic field lines in Tokamaks is responsible for non-uniform heat and particle loadings in divertor plates positioned in the plasma column. The understanding (and possibly control) of such chaotic regions is thus important to the design of future Tokamak experiments.

The actual behavior of plasma particles and even of magnetic field lines can only be revealed through complicated models that try to include all factors of physical interest in a given Tokamak experience. A direct investigation of chaotic field lines in such hyperrealistic model could hide essential features of the problem, which are best displayed by simple models. The Tokamap is an outstanding example of two-dimensional, area-preserving map which is nevertheless capable to convey some features of more complicated situations. We thus used the Tokamap in this work to investigate the field line escape by exits carved on the midst of the chaotic region. One virtue of the Tokamap is that all nonlinear behavior can be tuned up by varying a single parameter (k).

We already expect a complex structure for the escape basins and their boundary, since the latter is the closure of the stable manifold of the chaotic saddle, which is a non-attracting invariant set underlying a chaotic orbit in the phase space. This complexity is directly related to the final-state uncertainty: if the escape basins are much intertwined, it turns out to be almost impossible to predict to what exit will a given initial condition asymptote. We remark that this kind of uncertainty is completely different from the usual interpretation given to chaotic orbits: a final-state uncertainty is essentially due to the fractality of the escape basin boundary.

However, the use of an uncertainty dimension has shown not enough to disclose the dependence of the complexity, since the boundary is practically area-filling irrespective of the value of the parameter k. In this context, an extremely valuable alternative is the basin entropy and basin boundary entropies introduced by Sanjuán and collaborators. A zero entropy value would indicate no uncertainty at all, whereas a limiting value ($\log 2$) corresponds to a completely uncertain final state, when the escape basins are extremely fractal. Indeed, we have found that both entropies have a trend to increase with k, until they saturate close to the limit value of $\log 2$.

Our results, although obtained with the help of a simple map, shed some light on the general problem of final-state uncertainty of complex plasmas. Even for weak or moderate nonlinearities, the existence of a chaotic saddle with a fractal invariant manifold structure is enough to produce escape basins so complicated that it will be virtually unfeasible to determine in advance to which exit will a given initial condition escape to. This is even more dramatic when three or more exits are considered, since the corresponding exit basins can be shown to present the so-called Wada property: some fraction of the initial conditions belong to boundaries that contain points of all basins in their neighborhoods, no matter how small. This non-trivial property is a direct consequence of the manifold structure as well.

Acknowledgments

This work has been supported by grants from the Brazilian Government Agencies CNPq (proc. 301019/2019-3, 140713/2020-4), CAPES (proc. 88887.320059/2019-00), and FAPESP (grant 2018/03211-6).

References

[1] Horton, W. and Benkadda, S. (2015), *ITER Physics*, Singapore: World Scientific.
[2] IAEA (2002), *ITER Technical Basis*, ITER EDA Documentation Series No. 24. Vienna: International Atomic Energy Agency.
[3] Post, D.E. and Behrisch, R. (2013), *Physics of Plasma-Wall Interactions in Controlled Fusion*, Springer Science & Business Media.
[4] Federici, G., Andrew, P., Barabaschi, P., Brooks, J., et al (2003), Key ITER plasma edge and plasma-material interaction issues, *Journal of Nuclear Materials*, **313**, 11-22.
[5] Cordey, J.G. and Goldston, R.J. (1992), Progress toward a tokamak fusion reactor, *Physics Today*, **45**(1), 22-30.
[6] Bertolini, E., Celentano, G., Last, J.R., Tait, J., et al (1992), The JET divertor coils, *IEEE Transactions on Magnetics*, **28**(1), 275-278.
[7] Lipschultz, B., LaBombard, B., Terry, J.L., Boswell, C., and Hutchinson, I.H. (2007), Divertor physics research on Alcator C-Mod, *Fusion Science and Technology*, **51**(3), 369-389.
[8] Abdullaev, S.S. and Finken, K.H. (1998), Widening the magnetic footprints in a poloidal divertor tokamak: a proposal, *Nuclear Fusion*, **38**(4), 531-544.
[9] Jakubowski, M.W., Evans, T.E., Fenstermacher, M.E., Groth, M., Lasnier, C.J., Leonard, A.W., Schmitz, O., Watkins, J.G., Eich, T., Fundamenski, W., and Moyer, R.A. (2009), Overview of the results on divertor heat loads in RMP controlled H-mode plasmas on DIII-D, *Nuclear Fusion*, **49**(9), 095013.
[10] Jakubowski, M.W., Abdullaev, S.S., Finken, K.H., Lehnen, M., and Team, T. (2005), Heat deposition patterns on the target plates of the dynamic ergodic divertor, *Journal of Nuclear Materials*, **337**, 176-180.
[11] da Silva, E.C., Caldas, I.L., Viana, R.L., and Sanjuán, M.A. (2002), Escape patterns, magnetic footprints, and homoclinic tangles due to ergodic magnetic limiters, *Physics of Plasmas*, **9**(12), 4917-4928.
[12] Daza, A., Wagemakers, A., Georgeot, B., Guéry-Odelin, D., and Sanjuán, M.A. (2016), Basin entropy: a new tool to analyze uncertainty in dynamical systems, *Scientific Reports*, **6**(1), 1-10.
[13] Daza, A., Georgeot, B., Guéry-Odelin, D., Wagemakers, A., and Sanjuán, M.A. (2017), Chaotic dynamics and fractal structures in experiments with cold atoms, *Physical Review A*, **95**(1), 013629.
[14] Aguirre, J., Viana, R.L., and Sanjuán, M.A. (2009), Fractal structures in nonlinear dynamics, *Reviews of Modern Physics*, **81**(1), 333-386.

[15] Grebogi, C., McDonald, S.W., Ott, E., and Yorke, J.A. (1983), Final state sensitivity: an obstruction to predictability, *Physics Letters A*, **99**(9), 415-418.
[16] McDonald, S.W., Grebogi, C., Ott, E., and Yorke, J.A. (1985), Fractal basin boundaries, *Physica D: Nonlinear Phenomena*, **17**(2), 125-153.
[17] Balescu, R., Vlad, M., and Spineanu, F. (1998), Tokamap: A Hamiltonian twist map for magnetic field lines in a toroidal geometry, *Physical Review E*, **58**(1), 951-964.
[18] Mathias, A.C., Kroetz, T., Caldas, I.L., and Viana, R.L. (2017), Chaotic magnetic field lines and fractal structures in a tokamak with magnetic limiter, *Chaos, Solitons and Fractals*, **104**, 588-598.
[19] Morrison, P.J. (2000), Magnetic field lines, Hamiltonian dynamics, and nontwist systems, *Physics of Plasmas*, **7**(6), 2279-2289.
[20] Viana, R.L. (2000), Chaotic magnetic field lines in a Tokamak with resonant helical windings, *Chaos, Solitons and Fractals*, **11**(5), 765-778.
[21] Weyssow, B., Balescu, R., and Misguich, J.H. (1991), Chaotic diffusion across a magnetic island due to a single low-frequency electrostatic wave, *Plasma Physics and Controlled Fusion*, **33**(7), 763-793.
[22] Ferreira, A.A., Heller, M.V.A.P., Caldas, I.L., Lerche, E.A., Ruchko, L.F., and Baccalá, L.A. (2004), Turbulence and transport in the scrape-off layer TCABR tokamak, *Plasma Physics and Controlled Fusion*, **46**, 669-679.
[23] Castro, R.M., Heller, M.V.A.P., da Silva, R.P., Caldas, I.L., Degasperi, F.T., and Nascimento, I.C. (1997), A complex probe for measurements of turbulence in the edge of magnetically confined plasmas, *Review of Scientific Instruments*, **68**, 4418-4423.
[24] Portela, J.S., Caldas, I.L., and Viana, R.L. (2008), Tokamak magnetic field lines described by simple maps, *The European Physical Journal Special Topics*, **165**, 195-210.
[25] Lichtenberg, A.J. (1984), Stochasticity as the mechanism for the disruptive phase of the $m = 1$ tokamak oscillations, *Nuclear Fusion*, **24**, 1277-1289.
[26] Martin, T.J. and Taylor, J.B. (1984), Ergodic behaviour in a magnetic limiter, *Plasma Physics and Controlled Fusion*, **26**, 321-340.
[27] da Silva, E.C., Caldas, I.L., and Viana, R.L. (2002), Bifurcations and onset of chaos on the ergodic magnetic limiter mapping, *Chaos, Solitons & Fractals*, **14**, 403-423.
[28] Schelin, A.B., Caldas, I.L., Viana, R.L., and Benkadda, S. (2011), Collisional effects in the tokamap, *Physics Letters A*, **376**(1), 24-30.
[29] Balescu, R. (1998), Hamiltonian nontwist map for magnetic field lines with locally reversed shear in toroidal geometry, *Physical Review E*, **58**(3), 3781-3792.
[30] Freis, R.P., Hartman, C.W., Hamzeh, F.M., and Lichtenberg, A.J. (1973), Magnetic-island formation and destruction in a levitron., *Nuclear Fusion*, **13**(4), 533-548.
[31] Lichtenberg, A.J. and Lieberman, M.A. (1992), *Regular and Chaotic Dynamics*, 2nd. Ed. New York: Springer
[32] Filonenko, N.N., Sagdeev, R.Z., and Zaslavsky, G.M. (1967), Destruction of magnetic surfaces by magnetic field irregularities, Part II, *Nuclear Fusion*, **7**(4), 253-266.
[33] Poon, L., Campos, J., Ott, E., and Grebogi, C. (1996), Wada basin boundaries in chaotic scattering. *International Journal of Bifurcation and Chaos*, **6**(02), 251-265.
[34] Portela, J.S., Caldas, I.L., Viana, R.L., and Sanjuán, M.A. (2007), Fractal and Wada exit basin boundaries in tokamaks, *International Journal of Bifurcation and Chaos*, **17**(11), 4067-4079.
[35] Kroetz, T., Roberto, M., Caldas, I.L., Viana, R.L., Morrison, P.J., and Abbamonte, P. (2010), Integrable maps with non-trivial topology: application to divertor configurations, *Nuclear Fusion*, **50**(3), 034003.
[36] Péntek, A., Toroczkai, Z., Tél, T., Grebogi, C., and Yorke, J.A. (1995), Fractal boundaries in open hydrodynamical flows: Signatures of chaotic saddles, *Physical Review E*, **51**(5), 4076-4088.
[37] Jakubowski, M.W., Schmitz, O., Abdullaev, S.S., Brezinsek, S., Finken, K.H., Kramer-Flecken, A., and Textor, T. (2006), Change of the magnetic-field topology by an ergodic divertor and the effect on the plasma structure and transport, *Physical Review Letters*, **96**(3), 035004.
[38] Jakubowski, M.W., Abdullaev, S.S., Finken, K.H., and Textor, T. (2004), Modelling of the magnetic field structures and first measurements of heat fluxes for TEXTOR-DED operation, *Nuclear Fusion*, **44**(6), S1-S11.
[39] Evans, T.E., Roeder, R.K.W., Carter, J.A., Rapoport, B.I., Fenstermacher, M.E., and Lasnier, C.J. (2005), Experimental signatures of homoclinic tangles in poloidally diverted tokamaks, *Journal of Physics: Conference Series*, **7**(1), 015
[40] Abdullaev, S.S., Finken, K.H., Jakubowski, M., and Lehnen, M. (2006), Mappings of stochastic field lines in poloidal divertor tokamaks. *Nuclear Fusion*, **46**(4), S113.
[41] Evans, T.E., Roeder, R.K.W., Carter, J.A., and Rapoport, B.I. (2004), Homoclinic tangles, bifurcations and edge stochasticity in diverted tokamaks, *Contributions to Plasma Physics*, **44**(1-3), 235-240.